IEEE Access
Multidisciplinary ⋮ Rapid Review ⋮ Open Access Journal

Received 19 January 2023, accepted 5 February 2023, date of publication 13 February 2023, date of current version 21 February 2023.

Digital Object Identifier 10.1109/ACCESS.2023.3244402

RESEARCH ARTICLE

Investigating the Potential of Flexible Links for Increased Payload to Mass Ratios for Collaborative Robotics

GREET VAN de PERRE[1,2], THIERRY HUBERT[1,3], TOM VERSTRATEN[1,3], (Member, IEEE), AND BRAM VANDERBORGHT[1,2], (Senior Member, IEEE)

[1]Robotics and Multibody Mechanics Research Group, Vrije Universiteit Brussel, 1050 Brussels, Belgium
[2]IMEC, 3001 Leuven, Belgium
[3]Flanders Make, 3920 Lommel, Belgium

Corresponding author: Greet Van de Perre (Greet.Van.de.Perre@vub.be)

This work was supported by the Research Foundation Flanders (FWO) under Grant 12Z7920N, S001821N, 1505820N, and G0A9623N.

ABSTRACT One of the main restrictions of commercial cobots can be found in their limited payload to mass ratios. Flexible link manipulators seem to offer interesting advantages over traditional rigid robotics, in terms of lower self-weight, lower energy consumption and safer operation. However, the design and loading specifications in the general literature on flexible link manipulators differ from those expected in a collaborative industrial setting. In this paper, we want to investigate whether the use of flexible links can be truly beneficial for collaborative robotics. Firstly, the theoretical potential of flexible links to increase the payload to mass ratio is investigated. The feasibility to design a cylindrical flexible link for specific, realistic loading conditions is investigated, and the effect of link flexibility on the demanded motor torque and maximum reachable payload is visualised, while considering cylindrical links. Subsequently, to get insights in the accuracy and usability of such a manipulator, we experimentally quantify to what extent the undesired side effects of the flexible design can be counteracted using an appropriate controller. To comply with the envisioned application of collaborative robotics, a control strategy based on strain measurements along the link and robust to payload changes is proposed. The obtained accuracy was measured by tracking the end effector position using a Vicon motion capture system, considering two types of single link designs; firstly, a very flexible link setup with rectangular cross section, and secondly, a cylindrical flexible link, loaded to reach a payload to mass ratio of 1.

INDEX TERMS Collaborative robots, flexible links, lightweight robotics, strain-based control, vibration control.

I. INTRODUCTION

Collaborative robotics can help in fulfilling the increasing production flexibility demanded by the upcoming trend in mass customization. By merging human dexterity, flexibility and problem-solving ability with robotics strength, endurance and precision, the use of cobots can help in decreasing a worker's workload and at the same time increase the productivity. However, the economic attractiveness of a collaborative workstation is still limited, given their current limitations. One of the main issues lies in the limited payload to mass ratios. Table 1 lists the robot mass and maximum payload specifications for a selection of commercially available cobots, indicating in general a limited maximum payload with respect to their self-weight. The mass of the cobot however has a direct influence on the productivity in collaborative mode; as imposed by the standard ISO/TS 15066, to guarantee safety towards the human operator, the allowed operation speeds are restricted depending on, amongst others, the robot's moving mass. In addition, a high mass impedes the possibility of mounting the robot arm on a mobile platform.

The associate editor coordinating the review of this manuscript and approving it for publication was Okyay Kaynak.

Therefore, many approaches have been proposed in literature to decrease the robot's mass. On the one hand, this can be achieved by saving in actuator weight by e.g. using passive gravity compensation techniques [10], novel gearbox topologies [11] or off-joint actuation [12], [13]. Another strategy is to focus on reducing the structural mass. Traditional robots are designed with a sufficient stiffness of the links in order to minimize vibrations and to obtain a good positional accuracy at the end effector, resulting in voluminous and heavy designs. Commercial cobots are typically fabricated from aluminium. The use of lightweight materials with a higher specific stiffness, such as carbon-fiber-reinforced composites, can be a first approach to lower the robot's weight while still maintaining a significant structural stiffness. For the design of ANYpulator, Bodie et al. [14] used lightweight carbon fiber links, resulting in a payload to mass ratio of 1.04. Yin et al. [15] proposed a hybrid structure design approach to optimize lightweight robotic arms, combining carbon fiber reinforced plastic and aluminium parts. The use of composites unfortunately comes with a higher cost. Another -or combined- approach is therefore to focus on optimizing the link design and mass distribution of robotic links. Barrett et al. [16] designed a lightweight manipulator arm of 10 kg, with payload capability of 3 kg, using an aluminium exoskeletal design. Alternatively, topology optimization has been proven to be successful to lower the robot's weight to a certain extent, while still maintaining a significant structural stiffness [17], [18].

However, this stiffness constraint to assure good positional accuracy impedes a further decrease in structural mass. Therefore, for the design of the DLR LWR III [19], a novel approach was taken. Instead of ensuring positioning accuracy by a very rigid structure, the uncertainty introduced by the lightweight design is covered using an appropriate control. For assembly tasks, the target position is approximated on a millimetric scale until contact is detected, whereafter the exact assembly position is felt by a search movement using the integrated torque sensors; similarly as done by a human worker. This approach, in combination with high-power density actuation units and links in carbon fiber composites resulted in a design with a payload to mass ratio of 1.

The idea of lowering the rigidity of the robotic links can be extended to a higher degree when modelling the link flexibility and compensating the effect in an appropriate control strategy. As such, a significant additional weight reduction can be obtained. This type of manipulators is classified as flexible link robots and can be regarded as a class between the classical rigid robotics and soft continuum robots. A rough simulation in [20] revealed that, by shifting the deformation limit with a factor 10 with respect to that of traditional, rigid robots, a weight reduction of 94 % can be obtained. When allowing for higher deflections, the weight gain can be even further improved. The reduced structural mass will not only directly positively influence the safety and operation speed, in addition, smaller motor units are required to actuate the lightweight links, which again benefits the power consumption and overall robot mass.

The research on flexible link manipulators started as part of space research, given the specific concern of lightweight structures. Since then, many researchers have acknowledged the overall benefits of flexible link manipulators, namely the potential lower energy consumption, higher operation speeds, better transportability and safer operation, and have been focusing on modelling and formulating control strategies to counteract the undesired side effects of the link compliance. Indeed, because of the increased flexibility, configuration-dependent deflections will occur, whereas in addition, the structure will be more sensitive to vibrations. Different control strategies, both feedforward as feedback, have been proposed to suppress the vibrations and obtain accurate end effector positioning. Benosman and Le Vey [21], Rahimi and Nazemizadeh [22] and Dwivedy and Ebehard [23] provide good overviews of different control techniques that have been proposed for flexible link manipulators. Most studies investigated the behavior and control of a flexible link manipulator in the horizontal plane, excluding the effect of gravity. Different model-based control algorithms for flexible link manipulators have been proposed [24], [25], [26], [27]. On the other hand, model-free vibration control has been achieved using different techniques. Tokhi and Azad [28] used a high-pass filter to decouple the flexural dynamics from the rigid body dynamics in accelerometer measurements at the end effector, and used the obtained signal as input to a PID controller. Alternatively, different techniques based on strain sensing have been proposed. In [29], vibration control is achieved by direct strain feedback, using a set of strain gauges placed near the hub, while Ge et al. [30] proposed a nonlinear strain feedback strategy. In [31], a set of strain gauges is used to extract an indication of the end effector deflection. The rate of change of the derived signal is subsequently used as feedback signal. Less works consider motion in the gravity field, introducing joint configuration- and payload-dependent static deflections on top of the oscillations. Mansour et al. considers vibration suppression for motion in the vertical plane, using visual data from a camera mounted on the end effector [32]. On the other hand, Subedi et al. proposed a method to compensate the static deflection of a planar multi-link flexible manipulator using the feedback from inertial measurement units [33]. Malzahn et al. [34] compensates both effects by proposing a strain-based decentralized controller to damp out the structural vibrations in combination with a visual servoing controller as outer control loop to guarantee end effector tracking under gravity.

In the general literature on flexible link manipulators, the overall benefits of flexible link manipulators are only shallowly mentioned, while the focus is laid on modelling and counteracting the undesired side effects of the link flexibility. In this paper, however, we want to investigate whether flexible links can be feasible and truly beneficial

TABLE 1. Specifications of a selection of commercial cobots.

cobot type		av. repeatability (mm)	mass (kg)	max. payload (kg)	payload / mass
ABB	YuMi [1]	0.02	9.5	0.5	0.05
Universal Robotics	UR5 [2]	0.1	18.4	5	0.27
	UR10 [3]	0.1	28.9	10	0.35
	UR16e [4]	0.05	33.1	16	0.48
Franka Emika	Panda [5]	0.1	17.8	3	0.17
KUKA	iiwa 7 [6]	0.1	23.9	7	0.29
	iiwa 14 [7]	0.1	29.9	14	0.47
Fanuc	CR-7iA [8]	0.01	53	7	0.13
	CR-35iA [9]	0.03	990	35	0.04

in our field of interest, namely collaborative robotics. This targeted application will impose differences in cross section design and payload ratings then normally considered in the flexible link literature, and will influence the selection of the sensor system. As a first major contribution, we look at the theoretical potential of flexible links to increase the payload to mass ratio, by investigating the effect of the amount of link flexibility on the demanded motor torque and maximum reachable payload, while considering cylindrical links. While the general literature on flexible link manipulators considers homogeneous links with rectangular cross sections, whereby significant flexibility is only considered in the direction of motor motion, this is not interesting for cobots regarding both load capability as safety (because of sharp edges). In addition, in the literature, the introduced deflections are in general relatively high while only a very limited payload is considered. The demanded payloads in real industrial settings are in general significantly higher than those considered in the literature on flexible link robots. Therefore, we investigate the feasibility to design a cylindrical flexible link for a specific, realistic loading condition and study theoretically whether flexible links are indeed beneficial for increasing the payload to mass ratio.

Secondly, to get insights in the accuracy and usability of such a manipulator, we quantify to what extent the undesired side effects of the flexible design, considering both vibrations as gravity induced deflections, can be counteracted using an appropriate controller which is robust to highly varying payloads and feasible in industrial settings. While vision is often used in studies that include the effect of gravity [32], [34], the risk of occlusions makes a camera-based control strategy not always interesting in industrial settings. We therefore consider a control strategy based on strain measurements along the flexible link, and track the end effector position using a motion capture system, while considering a manipulator with payload to mass ratio of 1.

The paper is organised as follows; in section II, we visualise the effect of link flexibility on demanded motor torque and maximum reachable payload for a desired loading condition, as well as the potential of flexible links for increasing the payload to mass ratio. Subsequently, in section III we describe the control approach to compensate the flexural effects, relying on strain measurements along the flexible link and robust to varying payloads. In section IV, we measure to what extent the undesired flexural effects can be counteracted by the proposed strategy. Firstly, a very flexible link setup is considered, whereafter the strategy is implemented on a cylindrical flexible link, loaded to reach a payload to mass ratio of 1. Finally, a usecase is presented to demonstrate the robustness to varying payloads. The paper concludes by a conclusion and prospect to future work in section V.

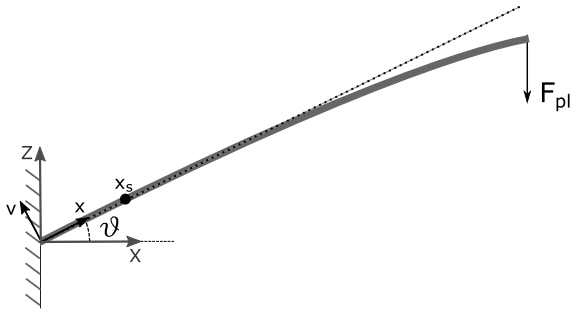

FIGURE 1. The link is modelled as a cantilever beam, clamped at an angle θ with the horizontal and featuring a payload at the end effector. x_s denotes the position of the set of strain gauges, considered in section III-C.

II. POTENTIAL OF FLEXIBLE LINKS FOR INCREASED PAYLOAD TO MASS RATIO

In general, cobots feature cylindrical shells as links, given the interesting load capabilities of hollow cylinders in combination with the overall maximised contact area, which is interesting to reduce the impact loads at collision. For a specified load condition, a model based on Euler-Bernouilli beam theory can provide interesting insights on the effect of varying the internal and external radius of a cylindrical shell.

The link can be modelled as a cantilever beam with length L, outer radius r_o and internal radius r_i, clamped at an angle θ with the horizontal (Figure 1). When considering pure bending, the equation of the elastic curve $v(x)$ can be

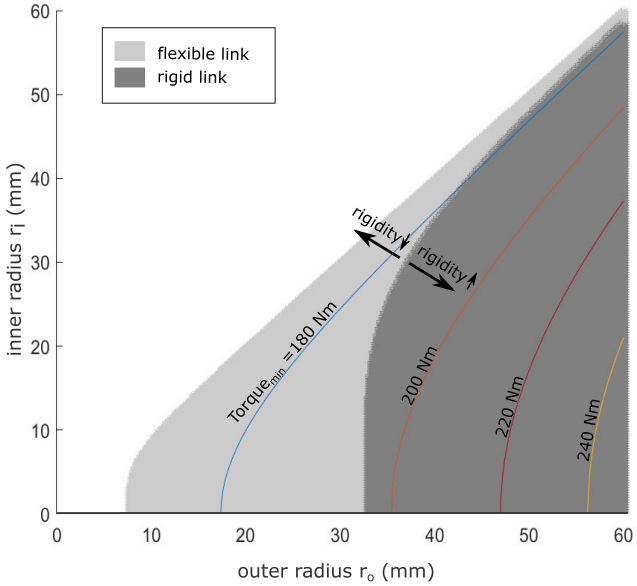

FIGURE 2. Effect of the outer radius r_o and inner radius r_i of a hollow cylindrical link on the static end effector deflection for specified payload; usecase for a single link with length of 0.5 m made of aluminium, considering a maximum payload of 14 kg and maximum angular acceleration of 15 rad/ s^2. To draw the line between rigid links, depicted in dark grey, and flexible links, depicted in light grey, a maximum deflection of 0.1 mm is selected. Coloured lines indicate the tendency of constant necessary motor torques to reach the desired imposed loading conditions.

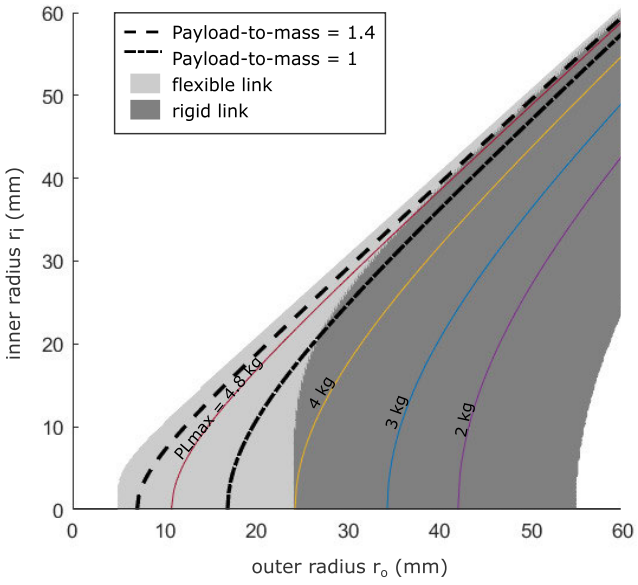

FIGURE 3. Effect of the outer radius r_o and inner radius r_i of a hollow cylindrical link on the static end effector deflection for a specified motor; usecase for a single link with length of 0.5 m made of aluminium and maximum angular acceleration of 15 rad/ s^2, actuated by a Tinsmith eRob110 motor with output torque of 62 Nm and weight of 3.3 kg. To draw the line between rigid links, depicted in dark grey, and flexible links, depicted in light grey, a maximum deflection of 0.1 mm is selected. Coloured lines indicate the tendency of constant values of maximum payload, while the thick, dotted lines give an indication of payload to mass ratio that can be reached.

calculated using the bending formula:

$$\frac{d^2v(x)}{dx^2} = \frac{M(x)}{EI_y} \tag{1}$$

with E the link's Young's modulus, and I_y the cross-section's area moment of inertia. $M(x)$ is the internal moment distribution at a distance x along the beam. For the following analysis, we consider the gravity-induced deflection, and are therefore interested in the internal moment distribution caused by gravity, which can be calculated as:

$$M(x) = -\left(\frac{F_g L}{2} + F_{PL} L\right) cos\theta + \left(F_g + F_{PL}\right) x\, cos\theta - \frac{F_g x^2}{2\,L} cos\theta \tag{2}$$

with F_g the gravitational force due to the link's self weight and F_{PL} the gravitational force due to a payload at the link's end effector. By substituting equation 2 in equation 1 and performing a double integration, the gravity-induced, static deflection at the end point of the link ($x = L$) can be obtained:

$$v_{tip} = -\frac{cos\theta}{EI_y}\left(\frac{F_{PL}L^3}{3} + \frac{F_g L^3}{8}\right) \tag{3}$$

As the deflection reaches a maximum value for $\theta = 0$, this case is considered for the following calculations. By substituting the formulas for the mass and the surface moment of inertia for a hollow cylinder, the deflection can be calculated as function of the outer radius r_o and internal radius r_i.

Figure 2 shows the results for a usecase for a single link with length of 0.5 m made of aluminium, considering a maximum payload of 14 kg and maximum angular acceleration of 15 rad/ s^2. In general, little information can be found on the stiffness specifications of commercial cobots. Therefore, to draw the line between rigid links, depicted in dark grey, and flexible links, depicted in light grey, a maximum deflection of 0.1 mm is chosen, which is a common value for the repeatability of an average commercial cobot platform (Table 1).[1]

In order to reach a rigid link design, the outer radius should be big enough; in this case higher than 33 mm, while the minimal thickness decreases for increased outer radius. The outer radius of typical commercially available cobots is located at the right boundary of the figure in order to reach the necessary desired stiffness of the structure; the Franka Emika Panda, for example, with maximum payload of 3 kg, has an average outer radius of 55 mm, whereas the UR16e, capable of carrying 14 kg, the outer radius is situated around 54 mm and 42 mm, for the first and second link respectively. Flexible links allow to significantly reduce the

[1] As the specific selection of this threshold can be questioned, we want to emphasis that we aim to focus on investigating overall trends and the effect of an increased structural flexibility. When adapting the threshold between rigid and flexible links, the observed trends, discussed below, remain valid, but evidently with a shifted boundary.

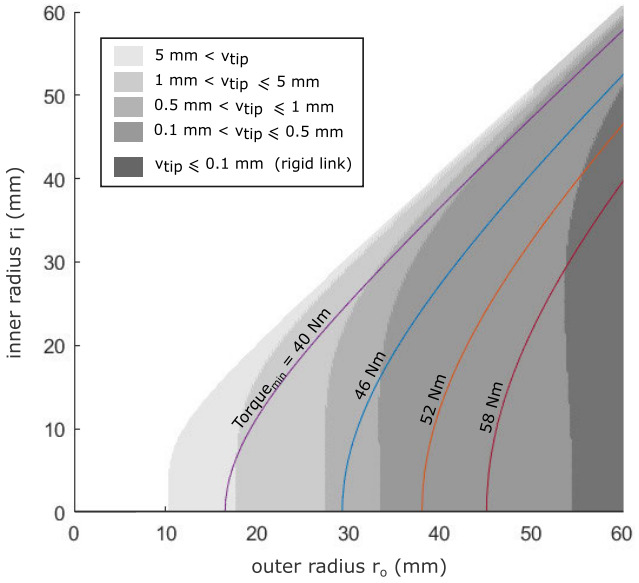

FIGURE 4. Effect of the outer radius r_o and inner radius r_i of a hollow cylindrical link on the static end effector deflection for specified payload; usecase for a single link with length of 0.5 m made of PVC, considering a maximum payload of 3 kg and maximum angular acceleration of 15 rad/ s^2. Variations in gray scale indicate regions of higher deflection, as clarified in the legend. Coloured lines indicate the tendency of constant necessary motor torques to reach the desired imposed loading conditions.

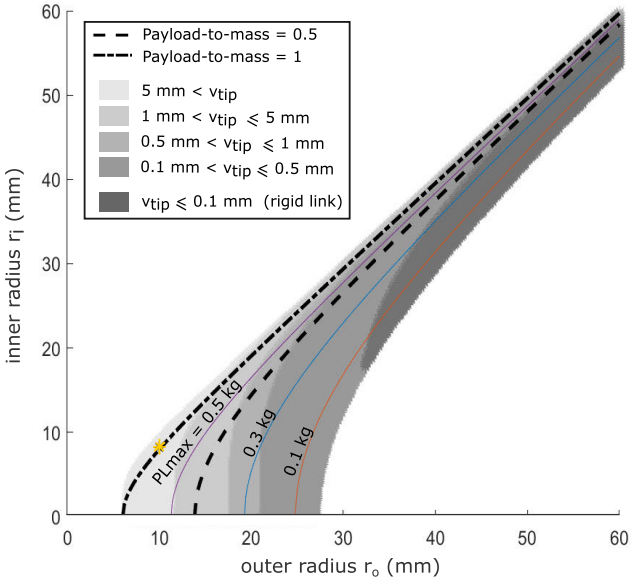

FIGURE 5. Effect of the outer radius r_o and inner radius r_i of a hollow cylindrical link on the static end effector deflection for a specified motor; usecase for a single link with length of 0.5 m made of PVC and maximum angular acceleration of 15 rad/ s^2, actuated by a Maxon EC motor-gearbox combination with output torque of 7.5 Nm and weight of 0.5 kg. Variations in gray scale indicate regions of higher deflection, as clarified in the legend. Coloured lines indicate the tendency of constant values of maximum payload, while the thick, dotted lines give an indication of payload to mass ratio that can be reached.

link's diameter and allow for a more slender design. It is clear that, when increasing the rigidity, and thus, the outer radius and thickness, the self weight of the structure will increase accordingly. Lines of constant necessary actuation torque to reach the desired imposed loading conditions, as function of the internal and external diameter, are superposed on Figure 2 using coloured lines. When allowing flexibility, the system can be actuated with an actuation unit of less than 180 Nm. When increasing the link rigidity, the necessary torque increases, and limited torque needs can only be achieved when considering a relatively large outer radius. As the weight of the motor will scale with its torque output, higher demanded torque will introduce heavier actuation units, and therefore decrease the possibility to reach interesting payload to mass ratios.

When starting from a selected actuation unit, a similar exercise on investigating the effect of the shell parameters can be performed. Figure 3 shows the results for a Tinsmith eRob110 motor with output torque of 62 Nm and weight of 3.3 kg, while again considering the same link length of 0.5 m and angular acceleration of 15 rad/ s^2. In this case, the calculated end-effector deflections to distinguish between rigid and flexible links are based on the maximum payload the motor can carry, on top of the link's self weight as specified by the internal and outer radius. The coloured lines show the tendency of constant values of maximum payload, while the thick, dotted lines give an indication of payload to mass ratio that can be reached, depending on the inner and outer radius. It is clear that, for a very rigid link structure, the maximum payload is limited, as most of the motor torque will be consumed by the self weight and inertia of the link itself. For very wide structures with high thickness, the self weight even exceeds the maximum capability of the selected motor, introducing the white area in the bottom right corner. When reducing the link stiffness, the maximum payload increases, as well as the payload to mass ratio. For a rigid link, a payload of more than 4.8 kg can be reached only for a geometry with large outer radius and small thickness. When considering flexible links, the same payload capability can be reached for smaller diameters. When allowing higher deflections, the maximum payload increases, together with the payload to mass ratio. A payload to mass ratio of 1 can here only be reached for rigid links when considering large outer radius and very small thickness, while the same values can be obtained for more slender designs when considering flexible links. When increasing the link flexibility, the payload to mass ratio increases to ratios up to 1.4.

Most commercial cobots are made of aluminium because of its interesting stiffness to weight ratio. Dropping the stiffness constraint and allowing for higher link deflections however could open the door for polymers, which, in general, have a lower specific stiffness, but also lower density and material cost.

Figure 4 visualises the results for a usecase for a link made of PVC, considering a maximum desired payload of 3 kg and, again, a maximum angular acceleration of 15 rad/ s^2. As for the previous examples, a link length of 0.5 m was

selected. Because of the reduced stiffness, compared to that of aluminium, and the combination of a relatively high link length and moderate payload, the boundary between flexible and rigid links is significantly shifted toward the right side. To reach a rigid link design for this case, the outer radius should be higher than 55 mm, whereas the minimal thickness is around 10 mm. In order to analyse the amount of introduced deflection, the region indicating flexible links is subdivided using different light grey shades. It can be noted that the outer diameter can be reduced by one third with respect to the value for a rigid design, while still maintaining a limited deflection at the end effector of maximum 0.5 mm. An additional decrease in outer radius or selecting a very thin design pushes the maximum deflection to higher values in the order of centimetres. Studying the necessary torques to actuate the system reveals that a reduced stiffness can decrease the torque demand up to 30 percent.

Figure 5 shows the results for a Maxon EC motor-gearbox combination with output torque of 7.5 Nm and weight of 0.5 kg, while again considering the same link length of 0.5 m, made of PVC and angular acceleration of 15 rad/ s^2. In this case, the limited motor torque significantly limits the maximum thickness of the structure, depending on the selected outer radius. It can be noted that, only for wide structures, a payload higher than 0.3 kg can be reached for a rigid design. Lowering the rigidity eventually results in an increased payload. In addition, as indicated by the dashed-dotted line, for this usecase, a payload to mass ratio of 1 can only be obtained for a flexible design.

When selecting an outer radius of 10 mm, one can see that, by lowering the thickness, the boundary of payload to mass ratio of 1 is crossed. The yellow asterix denotes a design with internal radius of 8.2 mm, which results in a geometry with a weight of 67 gram. The total manipulator weight therefore consists of 567 gram. The calculations indicate a maximum payload 577 gram, corresponding to a maximum payload to mass ratio slightly above 1. When considering the special case of payload to mass ratio of 1, and thus, a payload of 567 gram, a static deflection of 19 mm is expected.

III. STRAIN-BASED CONTROL

The use of flexible link manipulators inevitably introduces the need of a suitable control strategy to counteract the undesired side effects of the lightweight design, namely the introduced oscillations and the gravity-induced deflections.

Because of the flexibility, the end effector position control can no longer be obtained by solely using joint angle data. As elaborated in section I, different sensor systems have been proposed to capture the necessary data to represent the link's flexural behavior. Studies that include the effect of gravity mostly rely on vision. However, a camera-based control strategy is not always feasible in industrial settings, given the risk of occlusions. Therefore, in this paper, we present a control algorithm for flexible link manipulators under gravity, based on strain measurements. Combined with regular joint angle measurements, the strain measurements enable to sufficiently characterise the behavior of the flexible link manipulator, and the possibility of counteracting the undesired drawbacks of the flexible link design. Similarly as in [34], we propose a nested control strategy, whereby an inner loop is responsible for vibration control, whereafter the effect of the link compliance is limited to a configuration dependent static deflection, which is subsequently counteracted in an outer control loop.

The proposed controller is schematically represented in Figure 6. The control architecture is based on a central joint position controller to regulate the motor's angular position, visualised by the coloured region at the bottom left. To counteract the effects of the link's compliance, two distinct control loops work on different portions of the measured strain signal. Vibration control is achieved by proportional strain feedback [35], [36], based on the dynamic portion of the measured strain signal. As the resulting motion can be regarded as vibration-free, the remaining implications of the link compliance, i.e., the gravitationally induced deflections can be modelled using a simple static model, based on the static portion of the measured strain signal, and counteracted by compensating the joint position reference for the joint position controller. In what follows, the specific components of the global controller are discussed in detail.

A. JOINT CONTROL

Angular position control of the joint is achieved using a nested control structure, consisting of a PD position control loop G_{PD}, a PI velocity control loop G_{PI} and PID current loop. The block diagram of the joint controller is depicted in Figure 6 by the bottom-left coloured area. Given the high dynamics of the current control loop, it's not separately modelled but included in the motor representation G_{Motor}.

B. VIBRATION CONTROL

A proportional strain feedback strategy is used to dampen out the oscillations. Given the nested control architecture of the joint controller, the strain feedback signal can be inserted at different stages within this nested structure. To investigate the influence of the insertion point of the proportional strain feedback, the potential of increasing damping is investigated using a root locus plot, for both the input point of the position controller and the velocity controller. Figure 7(a) shows the close view of the root locus plot around the beam's first resonant frequency, for the proportional strain feedback inserted at the PD joint position control summation point, calculated using the transfer functions of the rectangular flexible beam setup discussed in section IV-A. As can be noted, the capability of increasing damping for this control configuration is very limited, as the complex pole pair originating from the beam's transfer function cannot significantly be pushed into region with higher damping. Figure 7 (b) visualizes the root locus for the strain feedback inserted at the joint velocity control summation point. Here, the damping can be significantly improved for increasing

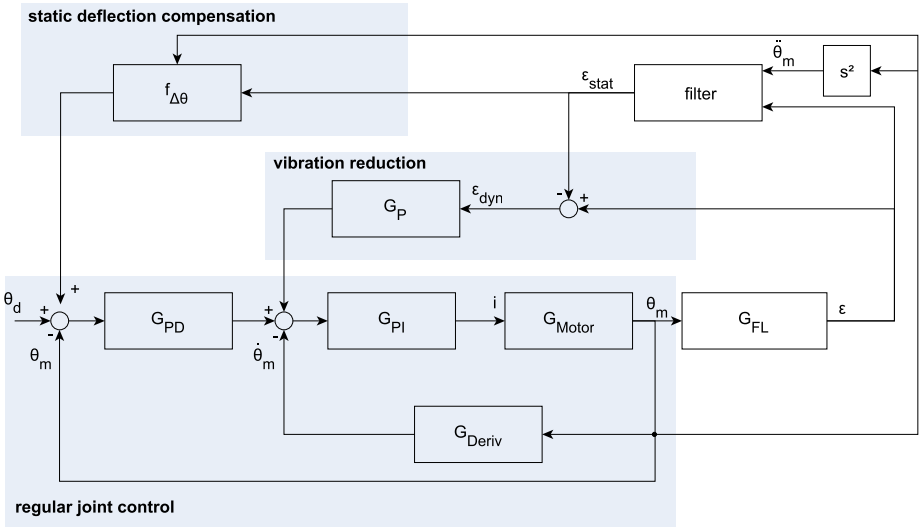

FIGURE 6. Schematic representation of the nested control scheme. The control architecture is based on a central joint position controller to regulate the motor's angular position, consisting of a PD position controller G_{PD}, with a nested PI velocity controller G_{PI} and PID current loop, jointly represented with the motor by G_{Motor}. Vibration control is achieved using a proportional controller G_P on the dynamic portion of the measured strain signal ϵ_{dyn}. The gravity induced static deflections are counteracted by compensating the joint position reference for the joint position controller, using a calculation of the predicted deflection from the static strain signal ϵ_{stat}, represented by $f_{\Delta\theta}$.

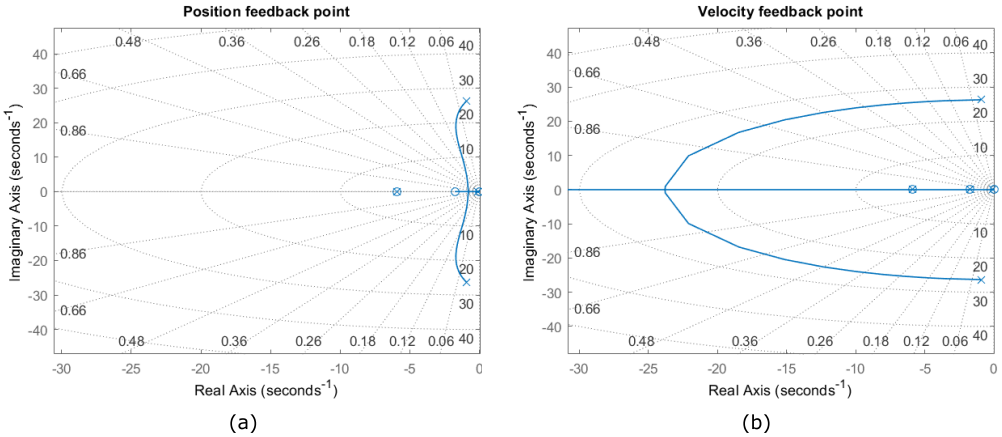

FIGURE 7. Root locus for strain feedback controller (a) at the position feedback input point (b) at the velocity feedback input point. The plots reveal that for (a) the proportional strain feedback cannot increase the damping significantly, while for (b), the complex pole pair can be shifted to regions with significant higher damping for increased values of the proportional gain.

values of the proportional strain gain. A similar conclusion was found by [37]. The strain feedback is therefore inserted at the velocity level summation point, as visualized in Figure 6.

C. GRAVITY INDUCED DEFLECTIONS

Because the vibrations are dampened out in the inner proportional strain feedback loop, the problem of end effector positioning reduces itself to counteracting the static deflections induced by gravity. This entails that in the resulting control loop, not the complete, complex dynamic model of the flexible link should be incorporated, but a simple static model suffices.

For a cantilever beam with length L, clamped at an angle θ with the horizontal, as visualised in Figure 1, the internal moment distribution $M(x)$ caused by gravity at a distance x along the beam can be calculated using formula 2, which is repeated here for the reader's convenience:

$$M(x) = -\left(\frac{F_g L}{2} + F_{PL} L\right) cos\theta + \left(F_g + F_{PL}\right) x\, cos\theta - \frac{F_g x^2}{2\,L} cos\theta \qquad (4)$$

with F_g the gravitational force due to the link's self weight and F_{PL} the gravitational force due to a payload at the link's end effector. The gravity-induced, static deflection at the

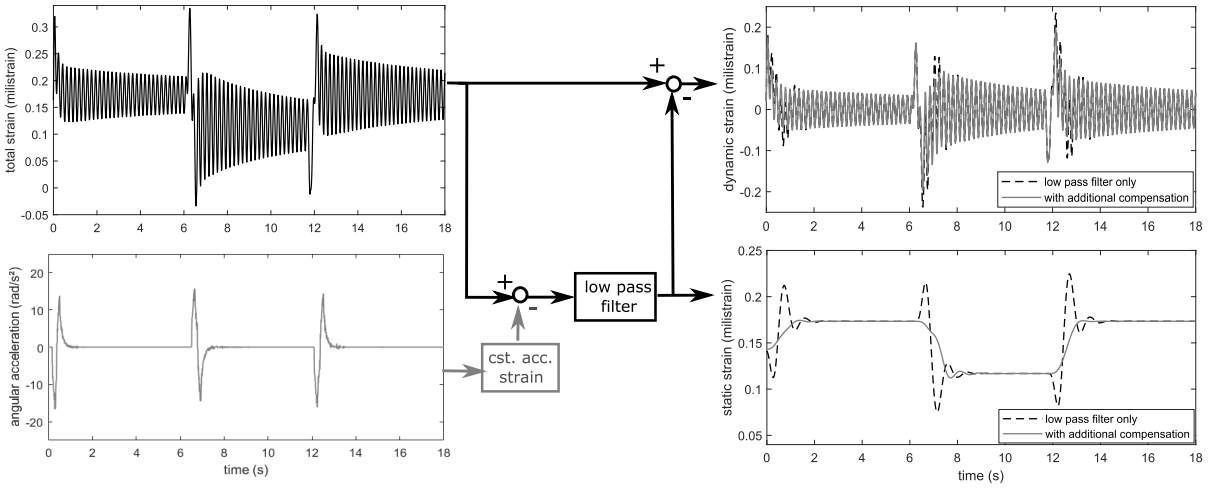

FIGURE 8. The measured strain signal is split into a gravitationally induced static component, and the portion corresponding to the vibrational behavior. When only using a low pass filter, the resulting static strain signal contains a portion of the motion-induced strain (black). Therefore, this portion is firstly subtracted from the total strain signal prior to the filtering process, to obtain a clean strain signal only reflecting the gravitational effect (grey).

end point of the link ($x = L$) was derived in section II by substituting equation 4 in the bending formula, given by equation 1, and performing a double integration:

$$v_{tip} = -\frac{cos\theta}{EI_y}\left(\frac{F_{PL}L^3}{3} + \frac{F_gL^3}{8}\right) \tag{5}$$

The strain $\epsilon(x)$ at the top surface of the link, introduced by the bending moment can be calculated as:

$$\epsilon(x) = -\frac{M(x)c}{EI_y} \tag{6}$$

with c the distance between the neutral line and the link's surface.

Substituting $M(x)$ by equation 4 yields:

$$\epsilon(x) = \frac{cos\theta\ c}{EI_y}\left(\left(\frac{F_gL}{2} + F_{PL}L\right) - \left(F_g + F_{PL}\right)x + \frac{F_gx^2}{2\,L}\right) \tag{7}$$

By solving this equation for F_{PL}, and substituting this in equation 5, a relationship between the deflection at the tip v_{tip} and the strain $\epsilon(x_s)$ at a specific location x_s along the link, independently of a possible payload, can be obtained:

$$v_{tip} = -\frac{L^3\epsilon(x_s)}{3(L - x_s)c} + \frac{F_gL^2\cos\theta}{24EI_y}(L - 4x_s) \tag{8}$$

The vertical offset due to the deflection can then finally be calculated as:

$$v_Z = v_{tip} \cdot cos\theta \tag{9}$$

D. FILTERING OF THE STRAIN SIGNAL

As the overall control loop is based on feedback of two distinct portions of the strain signal, a good filtering of the complete signal into the two desired components is necessary. The proportional strain feedback to counteract oscillations is based on the dynamic strain $\epsilon_{dyn}(x_s)$, i.e. the strain originating from the motion of the end effector. On the other hand, in the outer loop, equation 9 is used to calculate and counteract the vertical deviation of the end effector, based on the 'static strain' $\epsilon_{stat}(x_s)$, introduced by the bending moment originating from the gravitational forces. As for a given posture of the manipulator, the strain contribution caused by the gravitational moment is static, while the main portion of the dynamic strain will consist of an oscillating signal around the resonance frequencies, a low pass filter, with cut-off frequency below the link's first resonance frequency is a first logical attempt to extract the strain signal originating from the gravitational force from the overall strain signal measured by the strain gauges. This strategy is schematically visualised in black in Figure 8. The left top graph shows the total signal measured by the strain gauge bridge, when different steps are imposed on the motor position. The static strain, i.e. the strain originating from gravitational loads, should therefore follow a similar trend, and thus, should consist of different steps. The static and dynamic strain, obtained using low pass filtering are visualized in black in the bottom graphs. Using low pass filtering only, however, the resulting static strain signal will also contain the non-periodic contribution of the strain caused by the motor acceleration, reflected by the bumps in the static strain signal. Therefore, this portion is first subtracted from the total strain signal before passing it through the low pass filter.

This additional filtering action is schematically visualized in grey in the block scheme in Figure 8, while the static and dynamic strain obtained using this combined filtering process is visualised in grey in the bottom graphs of Figure 8. Except for a small overshoot, the resulting static strain now follows the desired trend by gradually increasing or decreasing from the initial strain value to the next one, corresponding to the imposed joint positions.

IV. END EFFECTOR ACCURACY

To obtain an indication of the end effector accuracy that can be achieved, the control strategy proposed in III was implemented and experimentally validated on a one link flexible manipulator by tracking the end effector position using a Vicon motion capture system. The frame of reference *XYZ* to express the end effector position is placed as visualized in Figure 1. To validate the control strategy for higher deflections and larger oscillations than can be reached with selected design for the Maxon EC-4pole30, denoted by the asterix in Figure 5 and discussed in section II, the control strategy was firstly validated on a very flexible system consisting of a rectangular shaped aluminium beam, following the general trend of the literature on flexible link manipulators. In a next step, the strategy was validated on the cylindrical design, considering the specific case of payload to mass ratio of 1. Finally, a small usecase is presented whereby the manipulator picks up a workpiece, brings it at a certain desired position at which a human operator performs an assembly task, whereafter the workpiece is released at a final position. Video's of the experiments can be accessed here.[2]

A. EXPERIMENTAL SETUP

The experimental setup is a one degree of freedom manipulator, actuated by an EC-4pole30 maxon motor, combined with a planetary gearbox with ratio 79:1. The angular position of the motor is measured by an incremental encoder at the motor side. The motor is controlled using an EPOS4 controller. The angular velocity and acceleration of the link were limited to values slightly higher than typical values of commercially available cobot platforms. The angular speed of the link was limited to π rad/s, while the speed limit of the elbow joint of the UR16e [4], KUKA iiwa [7] and Franka Panda [5] respectively equals π rad/s, 2.09 rad/s and 2.62 rad/s. For the test setup, a link speed of π rad/s corresponds to a tip speed of 1.5 m/s. The angular acceleration was limited to 15 rad/s^2, while the limit for the elbow joint of the Franka 12.5 rad/s^2.

The rectangular shaped flexible link consists of a 0.5 m aluminium beam with height of 0.002 m and width of 0.02 m. The link is mounted such that the width of the beam is aligned with the rotation axis of the motor. The connection part between the motor axis and the aluminium beam introduces an small additional increase in link length of 0.013 m. As the link's width is much larger than its height, only oscillations and deflections in the direction of the beam's height, and thus, perpendicular on the motor axis, are considered.

The cilindrical flexible link corresponds to the geometry denoted by the asterix in Figure 5 and discussed in section II; the link consists of a 0.5 m hollow cylinder from PVC, with outer and internal radius of respectively 0.01 m and 0.0082 m.

For both links, a pair of strain gauges is placed close to the motor hub, in a half-bridge Wheatstone configuration to only capture bending strain. Figure 9 shows the hardware setups, while Table 2 lists the most important specifications. The strain signals are captured using a Beckhoff data acquisition system and processed together with the motor data in Matlab Simulink using the TwinCAT environment [38] with a sample rate of 1 kHz.

[2]https://www.youtube.com/playlist?list=PLgNG89pNjzzKIGGGM0iTAd63qot9ypB8k

TABLE 2. Specifications of the hardware setup.

Actuation specifications		
Motor type	EC-4pole 30	
Gear ratio	79:1	
Imposed max speed	π rad/s	
Imposed max acc.	15 rad/s^2	
Link specifications		
Length (L)	0.5 m	
Material	aluminium	PVC
Cross section	rectangular width = 0.02 m thickness = 0.002 m	hollow circle outer radius = 0.01 m inner radius = 0.0082 m
Young's mod. (E)	69 Mpa	3 Mpa
Density (ρ)	2755 kg/ m^3	1310 kg/ m^3

B. CONTROLLER IMPLEMENTATION

As indicated in section III-A, the joint controller consists of nested control structure, including a PD position control loop, a PI velocity control loop and PID current loop. Both the current and velocity control loop of the joint controller are integrated in the EPOS4 controller and run at respectively 25 kHz and 2.5 kHz, while the position controller was integrated in Simulink, therefore running at the TwinCAT sampling rate of 1 kHz.

The gains for the current and velocity loop were obtained using the EPOS's auto tune function, while the position loop gains were experimentally selected to obtain a smooth step response without overshoot. Figure 10 visualizes the performance of the joint controller for the rectangular shaped flexible link setup.

C. RECTANGULAR SHAPED FLEXIBLE SETUP

Experiments were performed whereby step-like trajectories were imposed on the vertical coordinate of the end effector. Regular inverse kinematics for the rigid manipulator then resulted in the desired joint angle reference. Experiments were performed with and without payload, ranging up to 96 gram.

Figure 11 visualises the results of the proportional strain feedback controller. Figure 11 (a) shows the vertical coordinate of the end effector position captured by the Vicon system, while Figure 11 (b) visualises the measured strain signal. The grey signal depicts the measurements for a zero proportional gain, representing the baseline reference whereas the black curve shows the effect of the vibration controller. Without vibration control, an initial average overshoot in end effector position of 4 mm is detected. The structure only features a very limited damping effect, as the vibrations keep propagating with quasi constant amplitude. After 5 seconds, when a new position is imposed, the

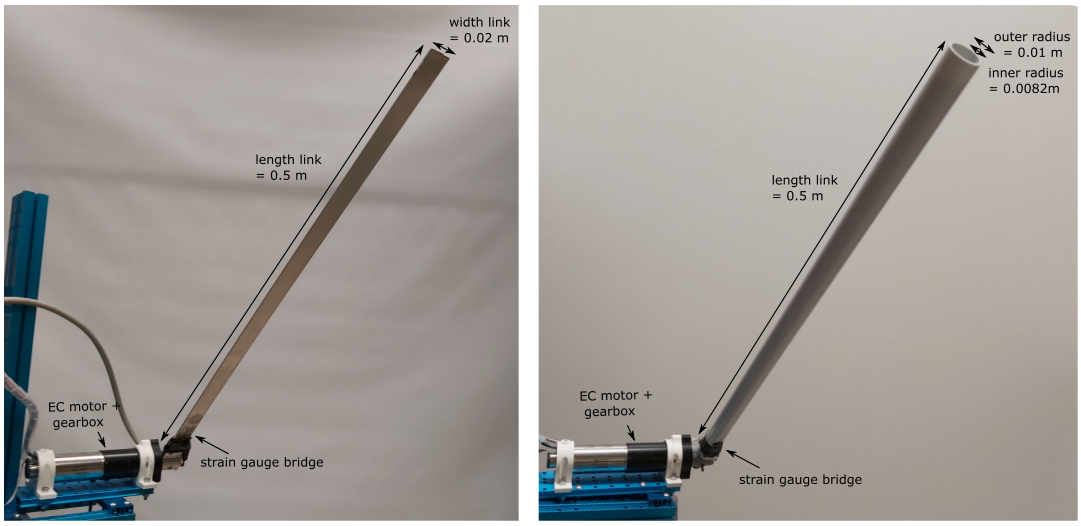

FIGURE 9. Experimental 1DOF flexible link setup (a) rectangular shaped flexible link, (b) cylindrical flexible link.

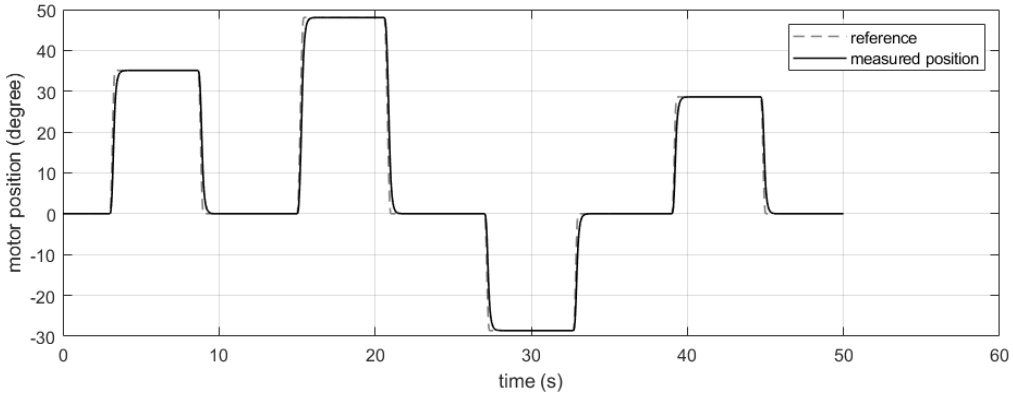

FIGURE 10. Performance of the joint position controller for different step responses, obtained for the rectangular shaped flexible link setup (no payload).

oscillation amplitude is still 3 mm. The beam's vibrational behavior is clearly reflected by the oscillations in the measured strain signal. The strain measurements clearly indicate that, when activated, the direct strain feedback controller succeeds in suppressing the dynamic strain very well, which results in a quasi vibration-free motion of the end effector, as visualised by the motion capture measurements.

The effect of outer control loop to counteract the gravity induced deflections is visualized in Figure 12. The imposed end effector trajectory consists of different steps and is depicted by a dashed line. Figure 12(a) visualises the complete trajectory sequence, while Figure 12(b) shows an enlarged view of the first step. Without static strain compensation, depicted in grey, an offset from the desired end effector position is noted, which depends of the exact configuration of the manipulator as described by equation 3. The offset is the most significant at $Z = 0$ mm, as this corresponds to the situation where the link is placed horizontally ($\theta = 0°$). The deflection due to the self weight of the link, and thus the positional error at the end effector in that case equals 13 mm. The measured end effector position with the outer control loop activated, is depicted in black. An average overshoot of 1.7 mm can be noted, and the steady state value is reached within 1.5 seconds. Comparison of the obtained measurement with the imposed reference indicates that the static deflections could be well compensated using the proposed control strategy, with a maximum relative steady state error of 0.004.

To investigate the robustness of the controller to payloads, different weights were placed at the end effector and the same end effector trajectories were imposed. Figure 13 groups the results for a payload of 96 gram. The baseline measurement, depicted in light grey in Figure 13, is obtained by disabling both the vibration controller as the static deflection compensator. When adding additional weight, the resonance frequencies of the combined flexible system are expected to decrease with respect to the resonance frequency

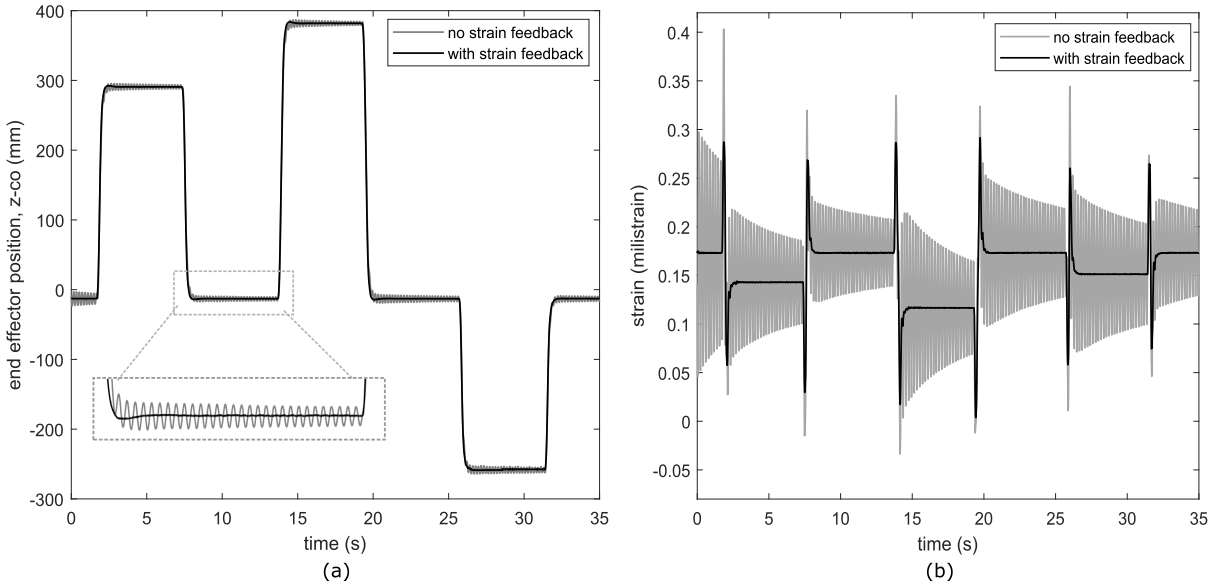

FIGURE 11. Results of the proportional strain feedback controller for different steps in joint angle reference for the rectangular shaped flexible link setup (without payload). Black: strain feedback enabled, grey: no strain feedback (baseline). (a) Vertical coordinate of the end effector position captured by the Vicon measurement system, (b) measured strain signal.

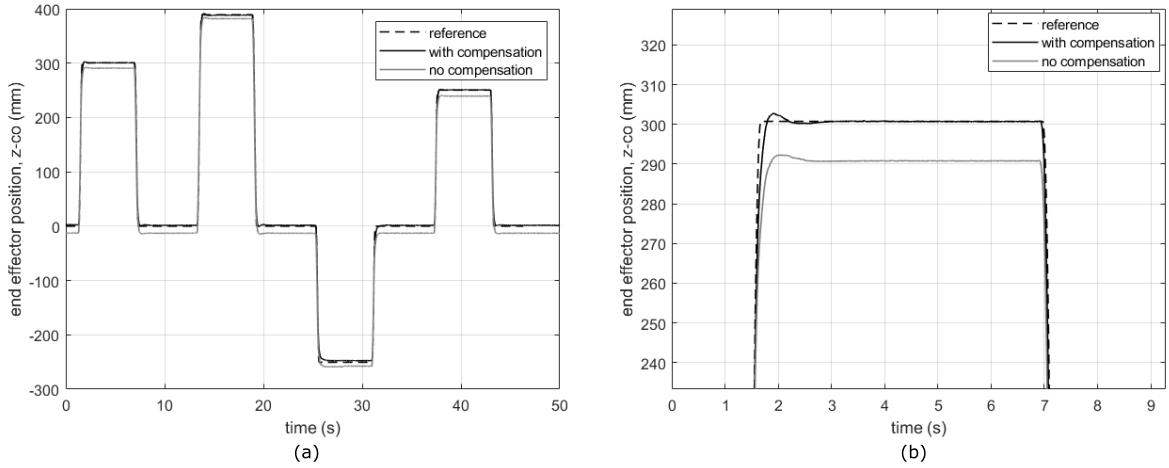

FIGURE 12. Results of the static deflection compensation algorithm for different steps in end effector position for the rectangular shaped flexible link setup (without payload). Dashed line: end effector reference, black: measured position with compensation algorithm activated, grey: measured position without compensation (baseline). (a) Complete trajectory sequence, (b) enlarged view of the first step.

of the plain link. FFT's of the measured strain signals indeed indicate a first fundamental frequency $f_1 = 1.87$ hz when incorporating a payload of 96 gram, with respect to a value of 4.2 hz for the non-loaded link. Because of the additional weight at the tip, the magnitude of the resulting oscillations is significantly larger then those encountered without payload, now reaching an initial value in the order of 100 mm. As the vibration controller is model-free, no adaptations need to be done in the controller for varying payloads. The effect of the direct strain feedback is visualized by the dashed-dotted signal. As for the payload-free case, a good and fast suppression of the end effector vibrations is obtained. As no static deflection compensation is performed yet, a configuration-dependent steady state error can be noted. The maximum error detected in this case equals 76 mm. Finally, the black signal depicts the results when the complete control system is enabled. The gravity induced deflections could be counteracted well with a maximum relative steady state error of 0.003, which indicates the robustness of the compensation strategy to counteract gravitational deflections for different payloads.

D. CYLINDRICAL LINK SETUP WITH PAYLOAD TO MASS RATIO OF 1

A similar strategy was followed to validate the control algorithm on the cylindrical flexible link. A payload of

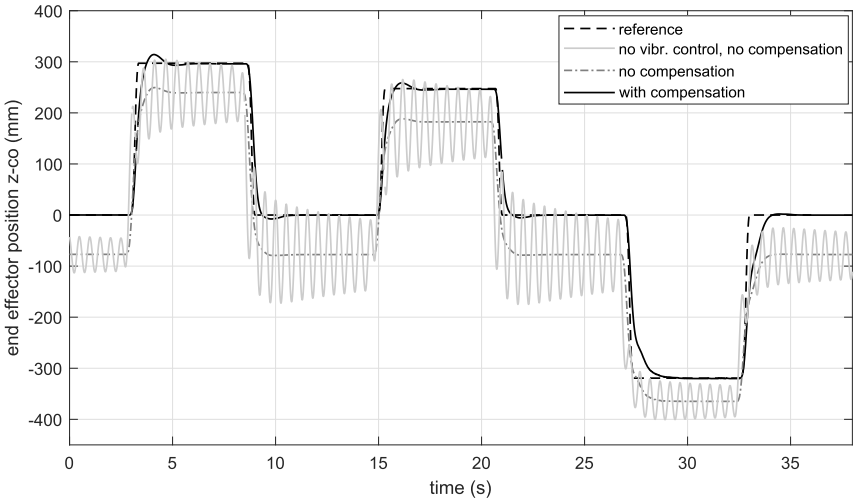

FIGURE 13. Results of the control algorithm for different steps in end effector position for the rectangular shaped flexible link setup with payload of 96 gram. Dashed black line: end effector reference, grey: measured position without compensation and without vibration control, grey dashed-dotted: with vibration control activated, but without static deflection compensation, black: measured position with complete controller activated.

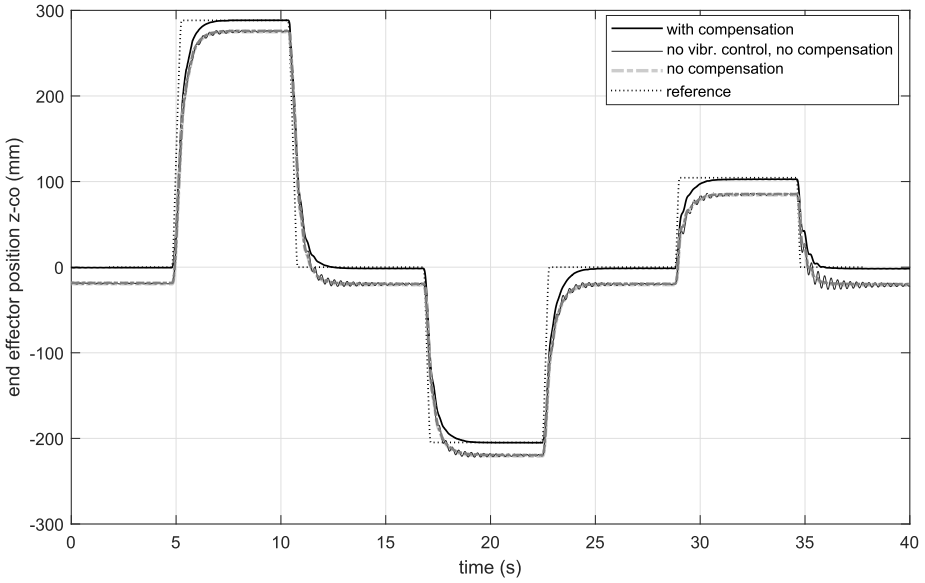

FIGURE 14. Results of the control algorithm for the cylindrical flexible link setup, for different steps in end effector position with 567 gram payload (= Payload to mass ratio of 1). Dotted black line: end effector reference, thin black: measured position without compensation and without vibration control, grey dashed-dotted: with vibration control activated, but without static deflection compensation, thick black: measured position with complete controller activated.

567 gram was attached to the manipulator's end effector, reaching a payload to mass ratio of 1. Figure 14 shows the measured end effector trajectories for this setup. The desired step-like trajectory is visualised by the dotted line. The reference measurement, i.e., the captured end effector trajectory when disabling the vibration controller and gravity compensation, is visualised by the thin black line. It can be noted that the effect of vibrations is less present as for the rectangular shaped flexible link, as could be expected from the increased stiffness resulting from the cylindrical design. The effect of the vibration controller is visualised by the grey dashed-dotted line. A maximum steady state error of 19 mm can be detected. When activating the static deflection compensation, as depicted by the thick black line, this error could be reduced to a maximum value of 1 mm.

E. USECASE

As last validation, we consider a usecase whereby the cylindrical flexible link setup picks up a workpiece, brings it to a desired position where an assembly process is performed,

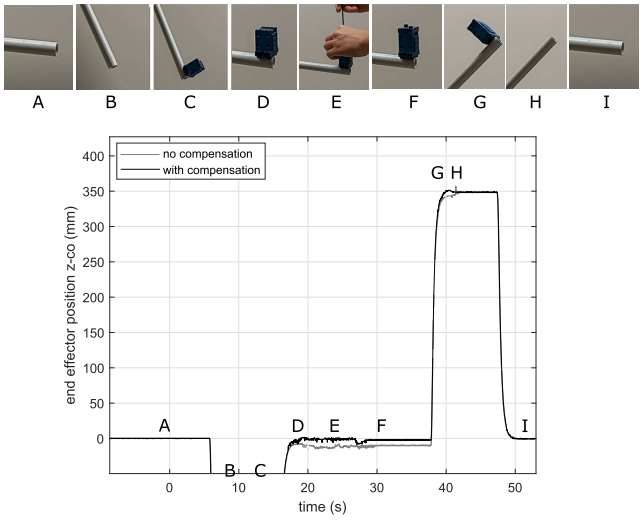

FIGURE 15. Use case for the cylindrical flexible link setup. Top: visualisation of the different steps of the usecase. Bottom: measured end effector positions with and without deflection compensation, respectively depicted in black and grey.

subsequently offers it to a position where the payload is released, whereafter the manipulator goes back to its initial position. With this usecase we aim to focus on investigating the effect of the variation in payload introduced in the different steps. The top part of Figure 15 visualises the different steps of the usecase, while the bottom part shows a zoomed view of the measured end effector trajectory with and without activation of the deflection compensation depicted in, respectively, black and grey. At the start of the usecase, at time A, the manipulator is placed horizontally, at $\theta = 0°$. As no payload is present, the deflection for this setup is rather small, namely 0.8 mm. Therefore, no clear visible distinction can be made when the compensation is activated or deactivated. At time B, the manipulator moves to $\theta = -80°$, where a workpiece of 110 gram is attached to the end effector at time C. At time D, the manipulator is again placed at $\theta = 0°$. Subsequently, a top part is assembled to the workpiece, slightly increasing the mass of the total workpiece to 123 gram. This region is indicated by E, where the effect of the assembly process is reflected in the fluctuations in end effector position. At time F, the assembly process is finished. In contrast to the situation at time A, the presence of the payload now introduces a higher deflection, which results in a notable distinction of end effector position with and without compensation. At time G, the manipulator is placed at $\theta = 45°$ wherafter at time H, the payload is released from the manipulator. When considering the case without deflection compensation, the release of the payload results in an increase of end effector position, because of the change in deflection. For the case with compensation, however, we can conclude that, except for a small overshoot, the end effector position is held constant, which illustrates the potential of compensating the deflection for changing payloads. Because without payload, the deflection is negligible, the end effector positions with and without compensation coincide starting from that time instant. At time I, the manipulator is again placed at the starting position, at $\theta = 0°$, where the effect of the deflection stays negligible.

V. CONCLUSION AND FUTURE WORK

In this paper, we investigated the potential of flexible links for increasing payload to mass ratios for collaborative robots. We started by visualising the effect of link flexibility on demanded motor torque and maximum reachable payload for a desired loading condition, as well as the potential of flexible link manipulators to increase the payload to mass ratio. While most literature on flexible links considers rectangular cross sections, this is not interesting for collaborative manipulators. Therefore, we focused on hollow cylindrical links and plotted the data as function of the outer and internal radii. For a selected motor unit, we were able to design a manipulator with payload to mass ratio of 1, which was only possible by considering flexible links. Subsequently, a strain-based control strategy for flexible link manipulators was proposed. The challenge of obtaining good positional end effector tracking was split into, on the one hand, the suppression of introduced vibrations, and on the other hand, the compensation of the residual static deflections introduced by gravity. This approach resulted in a nested control architecture, whereby vibration control is achieved by an inner, model-free, proportional strain feedback loop, while the outer loop provides the rigid body motion control by using a simple, static model to predict and counteract the current static end effector deflection from a single strain measurement along the link. Both main parts of the controller work on different contributions in the measured strain signal. Therefore, a good filtering technique to split the global strain signal in the dynamic component, corresponding to the oscillatory motion, and the static component, originating from the gravitational forces, is crucial. To quantify the accuracy of the end effector tracking, the proposed controller was implemented and experimentally validated on a one link flexible manipulator whereby the end effector position was measured using a Vicon motion capture system. In a first step, similarly like in the general flexible link literature, a very flexible setup with rectangular cross section was considered, while in a next step, the cylindrical flexible link setup with payload to mass ratio of 1, resulting from the initial theoretical study, was used. As final validation, we considered a usecase whereby the cylindrical flexible is used to pick up and release a workpiece, to demonstrate the effect of the compensation algorithm when changing the payload. The results show that, independently of the payload, the direct strain feedback successfully suppress the induced oscillations. In addition, the gravity-induced deflections could be compensated with a satisfying accuracy in steady state. While the necessary accuracy of a robot is of course very dependent on the exact task, within the specific field of collaborative robotics, the slightly reduced position

accuracy can in several situations be compensated by the presence of the human worker, or a impedance/force control strategy.

Future work includes extending the formulated models and algorithms towards multi-link manipulators, as well as going towards interaction strategies to allow safe collaboration with flexible link manipulators.

ACKNOWLEDGMENT

The authors would like to thank Dries Peumans for his help and valuable suggestions with respect to the signal processing and Hoang-Long Cao for his help with the experiments.

REFERENCES

[1] ABB. *Product Specification IRB 14050*. Accessed: Jan. 9, 2023. [Online]. Available: https://search.abb.com/library/Download.aspx?DocumentID=9AKK107046A3807&LanguageCode=en&DocumentPartId=&Action=LaunchProduct

[2] Universal Robotics. *Ur5 Technical Specifications*. Accessed: Jan. 9, 2023. [Online]. Available: https://www.universal-robots.com/media/50588/ur5_en.pdf

[3] Universal Robotics. *Ur10 Technical Specifications*. Accessed: Jan. 9, 2023. [Online]. Available: https://www.universal-robots.com/media/50895/ur10_en.pdf

[4] Universal Robotics. *Ur16e Technical Specifications*. Accessed: Jan. 9, 2023. [Online]. Available: https://www.universal-robots.com/media/1811483/ur16e-rgb-fact-sheet-landscape-a4.pdf

[5] F. Emika. *Panda Datasheet*. Accessed: Jan. 9, 2023. [Online]. Available: https://wiredworkers.io/wp-content/uploads/2019/12/Panda_FrankaEmika_ENG.pdf

[6] Kuka. *Datasheet LBR IIWA 7 R800*. Accessed: Jan. 9, 2023. [Online]. Available: https://www.kuka.com/-/media/kuka-downloads/imported/6b77eecacfe542d3b736af377562ecaa/0000246832_en.pdf?rev=9fea1d61304c4e0dbe4a92715453b34a&hash=9836BF804A5264E999481E642A45C010

[7] Kuka. *Datasheet LBR IIWA 14 R820*. Accessed: Jan. 9, 2023. [Online]. Available: https://www.kuka.com/-/media/kuka-downloads/imported/6b77eecacfe542d3b736af377562ecaa/0000246833_en. pdf?rev=be840bbedc414517b3d3636d15103350&hash=B14481D339D05007 C8489608111D928D

[8] Fanuc Corporation. *Datasheet CR-7IA*. Accessed: Jan. 9, 2023. [Online]. Available: https://www.fanuc.eu/-/media/files/pdf/products/robots/robots-datasheets-en/collaborative%20robots/datasheet-cr7ia-en.pdf?la=en

[9] Fanuc Corporation. *Datasheet cr-35IA*. Accessed: Jan. 9, 2023. [Online]. Available: https://www.fanuc.co.jp/en/product/catalog/pdf/robot/RCR-35iA(E)-02a.pdf

[10] D. Lee and T. Seo, "Lightweight multi-DOF manipulator with wire-driven gravity compensation mechanism," *IEEE/ASME Trans. Mechatronics*, vol. 22, no. 3, pp. 1308–1314, Jun. 2017.

[11] S. Crispel, P. L. Garcia, E. Saerens, A. Varadharajan, T. Verstraten, B. Vanderborght, and D. Lefeber, "A novel wolfrom-based gearbox for robotic actuators," *IEEE/ASME Trans. Mechatronics*, vol. 26, no. 4, pp. 1980–1988, Aug. 2021.

[12] D. Rodriguez-Cianca, C. Rodriguez-Guerrero, T. Verstraten, R. Jimenez-Fabian, B. Vanderborght, and D. Lefeber, "A flexible shaft-driven remote and torsionally compliant actuator (RTCA) for wearable robots," *Mechatronics*, vol. 59, pp. 178–188, May 2019.

[13] W. J. Marais and A. H. Göktogan, "Design and control of CRAM: A highly articulated cable-driven remote access manipulator for confined space inspection," in *Proc. Australas. Conf. Robot. Autom. (ACRA)*, 2017, pp. 1–9.

[14] K. Bodie, C. D. Bellicoso, and M. Hutter, "ANYpulator: Design and control of a safe robotic arm," in *Proc. IEEE/RSJ Int. Conf. Intell. Robots Syst. (IROS)*, Oct. 2016, pp. 1119–1125.

[15] H. Yin, J. Liu, and F. Yang, "Hybrid structure design of lightweight robotic arms based on carbon fiber reinforced plastic and aluminum alloy," *IEEE Access*, vol. 7, pp. 64932–64945, 2019.

[16] E. Barrett, E. M. Hoffman, L. Baccelliere, and N. G. Tsagarakis, "Mechatronic design and control of a light weight manipulator arm for mobile platforms," in *Proc. IEEE/ASME Int. Conf. Adv. Intell. Mechatronics (AIM)*, Jul. 2021, pp. 1255–1261.

[17] B. J. Kim, D. K. Yun, S. H. Lee, and G. W. Jang, "Topology optimization of industrial robots for system-level stiffness maximization by using part-level metamodels," *Struct. Multidisciplinary Optim.*, vol. 54, no. 4, pp. 1061–1071, Oct. 2016.

[18] X. Wang, D. Zhang, C. Zhao, P. Zhang, Y. Zhang, and Y. Cai, "Optimal design of lightweight serial robots by integrating topology optimization and parametric system optimization," *Mechanism Mach. Theory*, vol. 132, pp. 48–65, Feb. 2019.

[19] A. Albu-Schäffer, S. Haddadin, C. Ott, A. Stemmer, T. Wimböck, and G. Hirzinger, "The DLR lightweight robot: Design and control concepts for robots in human environments," *Ind. Robot, Int. J.*, vol. 34, no. 5, pp. 376–385, 2007.

[20] K. Merckaert, A. De Beir, N. Adriaens, I. El Makrini, R. Van Ham, and B. Vanderborght, "Independent load carrying and measurement manipulator robot arm for improved payload to mass ratio," *Robot. Comput.-Integr. Manuf.*, vol. 53, pp. 135–140, Oct. 2018.

[21] M. Benosman and G. Le Vey, "Control of flexible manipulators: A survey," *Robotica*, vol. 22, no. 5, pp. 533–545, 2004.

[22] H. N. Rahimi and M. Nazemizadeh, "Dynamic analysis and intelligent control techniques for flexible manipulators: A review," *Adv. Robot.*, vol. 28, no. 2, pp. 63–76, 2014.

[23] S. K. Dwivedy and P. Eberhard, "Dynamic analysis of flexible manipulators, a literature review," *Mech. Mach. Theory*, vol. 41, no. 7, pp. 749–777, 2006.

[24] G. G. Rigatos, "Model-based and model-free control of flexible-link robots: A comparison between representative methods," *Appl. Math. Model.*, vol. 33, no. 10, pp. 3906–3925, Oct. 2009.

[25] M. Moallem, R. V. Patel, and K. Khorasani, "Nonlinear tip-position tracking control of a flexible-link manipulator: Theory and experiments," *Automatica*, vol. 37, no. 11, pp. 1825–1834, Nov. 2001.

[26] A. Shawky, D. Zydek, Y. Z. Elhalwagy, and A. Ordys, "Modeling and nonlinear control of a flexible-link manipulator," *Appl. Math. Model.*, vol. 37, no. 23, pp. 9591–9602, Dec. 2013.

[27] I. Giorgio and D. Del Vescovo, "Non-linear lumped-parameter modeling of planar multi-link manipulators with highly flexible arms," *Robotics*, vol. 7, no. 4, p. 60, Sep. 2018.

[28] M. O. Tokhi and A. K. Azad, *Flexible Robot Manipulators: Modelling, Simulation and Control*, vol. 68. London, U.K.: IET, 2008.

[29] Z. Mohamed, J. Martins, M. Tokhi, J. S. Da Costa, and M. Botto, "Vibration control of a very flexible manipulator system," *Control Eng. Pract.*, vol. 13, no. 3, pp. 267–277, Mar. 2005.

[30] S. S. Ge, T. H. Lee, and G. Zhu, "Improving regulation of a single-link flexible manipulator with strain feedback," *IEEE Trans. Robot. Autom.*, vol. 14, no. 1, pp. 179–185, Feb. 1998.

[31] T. Mansour, A. Konno, and M. Uchiyama, "Modified PID control of a single-link flexible robot," *Adv. Robot.*, vol. 22, no. 4, pp. 433–449, Jan. 2008.

[32] T. Mansour, X. Jiang, A. Konno, and M. Uchiyama, "Experimental verification on vibration suppression of a flexible manipulator using MPID controller," in *Proc. IEEE Int. Conf. Robot. Autom.*, May 2008, pp. 2896–2901.

[33] D. Subedi, T. N. Aune, I. Tyapin, and G. Hovland, "Static deflection compensation of multi-link flexible manipulators under gravity," *IEEE Access*, vol. 10, pp. 9658–9667, 2022.

[34] J. Malzahn, A. S. Phung, and T. Bertram, "A multi-link-flexible robot arm catching thrown balls," in *Proc. 7th German Conf. Robot. (ROBOTIK)*. Munich, Germany: VDE, 2012, pp. 1–6.

[35] M. M. Tumari, M. Ahmad, M. Saealal, M. Zawawi, Z. Mohamed, and N. Yusop, "The direct strain feedback with PID control approach for a flexible manipulator: Experimental results," in *Proc. 11th Int. Conf. Control, Autom. Syst.*, 2011, pp. 7–12.

[36] J. Malzahn, M. Ruderman, A. S. Phung, F. Hoffmann, and T. Bertram, "Input shaping and strain gauge feedback vibration control of an elastic robotic arm," in *Proc. Conf. Control Fault-Tolerant Syst. (SysTol)*, Oct. 2010, pp. 672–677.

[37] J. Malzahn, "Modeling and control of multi-elastic-link robots under gravity," Ph.D. dissertation, Dept. Elect. Eng. Inf. Technol., TU Dortmund Univ., Germany, 2014.

[38] K. Langlois, T. Van Der Hoeven, D. R. Cianca, T. Verstraten, T. Bacek, B. Convens, C. Rodriguez-Guerrero, V. Grosu, D. Lefeber, and B. Vanderborght, "EtherCAT tutorial: An introduction for real-time hardware communication on windows [tutorial]," *IEEE Robot. Autom. Mag.*, vol. 25, no. 1, pp. 22–122, Mar. 2018.

GREET VAN de PERRE received the degree in mechanical engineering from Vrije Universiteit Brussel, in June 2011, and the Ph.D. degree in social robotics, in 2018. She is currently a Postdoctoral Researcher and an Associate Professor with the Robotics and Multibody Mechanics Research Group, Vrije Universiteit Brussel. She is also working on flexible link manipulators for collaborative robotics, funded by an Research Foundation—Flanders (FWO) Junior Postdoctoral Fellowship. She was granted a scholarship from the FWO, for her Ph.D. degree. Her research interests include human–robot interaction, collaborative robotics, and lightweight robotics.

THIERRY HUBERT received the master's degree in industrial engineering from Vrije Universiteit Brussel, in July 2020, where he is currently pursuing the Ph.D. degree with the Robotics and Multibody Mechanics Research Group. His research interest includes the weight optimization of robotic structures without stiffness constraints.

TOM VERSTRATEN (Member, IEEE) received the master's degree in electromechanical engineering and the Ph.D. degree from Vrije Universiteit Brussel (VUB), in 2012 and 2018, respectively. He worked as a Visiting Researcher at TU Darmstadt, Germany, for a period of four months, in 2017, and The University of Tulsa, Tulsa, OK, USA, for a period of eight months, from 2018 to 2019. He is currently a Professor with the Robotics and Multibody Mechanics Research Group, VUB. His research interests include the study and development of energy-efficient actuators for applications with varying loads and speeds, elastic actuators, and redundant actuation. He was awarded fellowships of the Research Foundation—Flanders (FWO) for his doctoral and postdoctoral research. For this research stay, he was awarded the Fulbright Grant for visiting scholars.

BRAM VANDERBORGHT (Senior Member, IEEE) is currently a Professor with the Robotics and Multibody Mechanics Research Group, Vrije Universiteit Brussel. He did a research stay at AIST, Japan. He was a Postdoctoral Researcher at IIT, Italy, and a Research Director at UBB, Romania. He had an ERC Starting Grant and coordinates the EU FET Project SHERO on self-healing soft robots and EU Marie Currie ITN SMART on smart self-responsive materials for soft robots. His research interests include cognitive and physical human–robot interaction, robot assisted therapy, humanoids, assistive robotics, and cobots with the core technology of using variable impedance actuators and self-healing actuators.